PCCP

Electron passivation in CaF_2 on calcium metal anodes

Journal:	*Physical Chemistry Chemical Physics*
Manuscript ID	CP-ART-05-2022-002274.R1
Article Type:	Paper
Date Submitted by the Author:	04-Sep-2022
Complete List of Authors:	Batzinger, Kevin; Binghamton University, Physics Smeu, Manuel ; Binghamton University, Physics

PCCP

ARTICLE TYPE

Cite this: DOI: 00.0000/xxxxxxxxxx

Electron passivation in CaF_2 on calcium metal anodes

Kevin Batzinger[a] and Manuel Smeu[a*]

Received Date
Accepted Date

DOI: 00.0000/xxxxxxxxxx

Current electrolytes in calcium-ion batteries suffer from a lack of stability and degradation caused by reduction from the anode. The solid-electrolyte interphase (SEI) that forms on the anodes during operation stems the flow of electrons from the anode to the electrolyte. CaF_2 is a common inorganic compound found in the SEI, and is derived from electrolyte salts such as $Ca(PF_6)_2$. CaF_2 can exist in crystalline, polycrystalline, and amorphous phases in the SEI, and as recent work has shown, different phases of the same compound can have vastly different electronic conductivities. Using the non-equilibrium Green's function technique with density functional theory (NEGF-DFT), we find that amorphous phase systems enhance electron tunneling in thin CaF_2 films by 1-2 orders of magnitude when compared to crystalline and polycrystalline CaF_2 systems. Transport through several amorphous structures was considered showing that, despite their random structures, their conductance properties are similar. Through analysis of the decay constant β and the low-bias conductance of each system, we show that crystalline and polycrystalline CaF_2 offer greater protection of the electrolyte than amorphous CaF_2.

1 Introduction

Lithium-ion batteries (LIBs) are costly to produce due to their reliance on rare metals, they have safety concerns associated with them, and have specific energies that are approaching the limit that can be attained in conventional electrochemical cells.[1,2] Due to this, alternatives to current lithium-ion batteries must be found. Multivalent ion batteries (MVIBs) are emerging technologies that employ ions such as Ca^{2+} or Al^{3+} in place of Li^+.[3] Despite the larger mass of the ions in MVIBs, they can shuttle multiple charges per ion, allowing for batteries with similar energy densities to LIBs that are manufactured using materials that are abundant in the Earth's crust.[4–6] In this regard, MVIBs have an advantage over conventional LIBs; calcium, for example, is the fifth most abundant element in the Earth's crust, while lithium is 33rd.[6] As well, lithium mining has several geopolitical concerns associated with it.[4,7] The fact that calcium is so abundant means that the sourcing of materials for calcium-ion batteries (CIBs) would be cheaper and more environmentally friendly than for LIBs.[4] However, calcium-ion batteries have not yet been commercially realized, in part due to a lack of stable electrolytes.[8]

Many liquid electrolytes used in batteries decompose during operation due to electron transfer from the anode to the electrolyte.[8–11] However, when this occurs, the decomposition products of the electrolyte form a protective layer on the surface of the anode, called the solid-electrolyte interphase (SEI). The SEI stems electron flow and protects the electrolyte from further decomposition, and consists of inorganic components close to the anode surface and organic fragments deposited further from the anode surface.[9–11] In CIBs the SEI consists of a variety of different compounds, including the inorganic compounds CaF_2, CaO, $CaCl_2$, and CaH_2, and organic compounds such as calcium carbonate.[10–12] This investigation focuses on the inorganic compound CaF_2. Previous work in our group on LIBs[13] has shown that electron conductance is greater in those regions of the SEI that contain an interface between two grains (commonly referred to as a grain boundary, hereafter referred to as a polycrystalline system), which stresses the importance of analyzing electron transport through the compounds that make up the SEI in all of the phases that they can form. This ensures a broad-spectrum evaluation of a prototypical component of the SEI and its properties. Therefore, CaF_2 was investigated in three different crystallographic phases: crystalline, amorphous, and polycrystalline. This investigation seeks to determine the effectiveness of different crystallographic phases of CaF_2 at reducing electron flow, and to help build a database of SEI components which are best able to stem electron flow from the anode in CIBs.[12]

[a]*Department of Physics, Binghamton University-SUNY, Binghamton, NY 13902, USA. E-mail: msmeu@binghamton.edu*

† Electronic Supplementary Information (ESI) available: Comparative transmission spectra for Ca with various amounts of strain; amorphous CaF_2 structures generated via the liquid quench technique; information about the band gap of each CaF_2 system; description of how grain boundaries impact the density-of-states of CaF_2; scattering state plots of varying thicknesses of crystalline CaF_2; scattering state plots of amorphous CaF_2 systems; information about the zero-bias conductance of each system; and information on the size of each system. See DOI: 10.1039/cXCP00000x/

2 Computational Methods

The Vienna *ab initio* Simulation Package (VASP)[14–17] was utilized to carry out structure relaxations and *ab initio* molecular dynamics (AIMD) simulations in order to produce crystalline, amorphous, and polycrystalline CaF_2 systems as well as the two-probe geometries used for the calculation of electron transport properties. We utilized projector augmented wave potentials with the Perdew-Burke-Ernzerhof generalized gradient approximation (PBE-GGA).[18,19] The energy cutoff was 500 eV and sufficient *k*-points were employed for the energy to be converged within 1 meV per atom. The relaxations were continued until forces on atoms were less than 0.02 eV/Å.

Because CaF_2 is harder than Ca, the two-probe structures were built such that CaF_2 preserved its crystal structure (with a lattice constant of 5.504 Å) while the Ca was strained to accommodate lattice mismatch.[20] This resulted in the *a* and *b* lattice vectors of Ca decreasing slightly, corresponding to a strain of 0.34%. Then the *c*-vector of the Ca metal cell was varied to find the *c* lattice vector with minimum energy. The resulting *c* lattice vector increased slightly, producing a strain of 1.47% along that direction. In order to ensure minimal effect on transmission calculations, the transmission spectra of each strained Ca electrode was calculated, and these data are shown in Fig. S1.† From these data, it is evident that straining the Ca electrodes does not significantly impact the transmission properties of the system. Crystalline CaF_2 was placed in between two strained Ca electrodes as shown in Fig. 1. The first two layers of Ca, shown in the red shaded region in Fig. 1, were held fixed, while the remaining atoms were free to relax. Because the CaF_2 region was previously relaxed, the lattice dimensions were fixed along the *a* and *b* directions but optimized along the *c* direction. Once the structure was optimized, the system was extended to build the two-probe structure shown at the bottom of Fig. 1, where the frozen Ca atoms in the red boxes are repeated as semi-infinite left/right electrodes, enclosed in the green boxes. This same approach was used for amorphous and polycrystalline systems. The naming convention for the different phases of CaF_2 are as follows: crystalline CaF_2 systems are referred to as "CaF_2" with the thickness of the CaF_2 layer in parenthesis (i.e., "CaF_2 (8.8 Å)"), amorphous CaF_2 systems are referred to as "a-CaF_2" with the thickness of the CaF_2 layer similarly in parenthesis (i.e. "a-CaF_2 (12.9 Å)"), and polycrystalline systems are referred to as "twist" and "mirror" systems, shown in Fig. 2. The twist system has two orientations, as shown in Fig. 2(d) and (e). These orientations are parallel and perpendicular to the electron transport direction, and hence the twist systems are called "twist perpendicular" and "twist parallel." The plane of the mirror grain boundary is parallel to the direction of electron transport, and hence is referred to as "mirror parallel." It should be pointed out that these systems may be at an unavoidable overpotential due to the geometry necessitated for the DFT calculations.[21,22] The voltage could be established by more sophisticated approaches such as including a vacuum in the simulation cell. For the current study, the relatively simple systems shown in Figs. 1 and 2 were employed for the electron transport calculation. The trends regarding leakage through crystalline, polycrystalline, and amorphous CaF_2 are likely to hold regardless of potential.

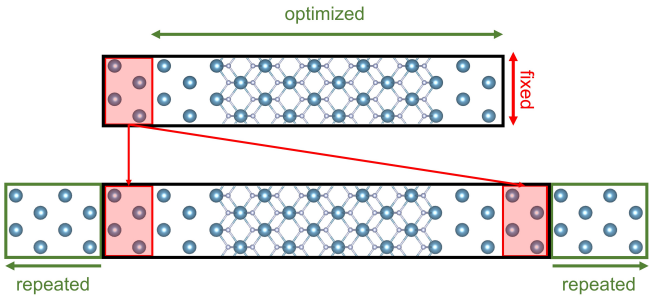

Fig. 1 Top: Example of a Ca/crystalline CaF_2 system used in structural relaxations. The cell was allowed to relax in the direction perpendicular to the interface (green arrow) and fixed to the lattice constant of CaF_2 in the plane of the interface. Two layers of Ca atoms (inside red box) were kept frozen in their strained positions while all other atoms were allowed to relax. Once relaxed, the two-probe structure (bottom) was constructed by extending the strained Ca regions to the left and right, shown in the green boxes.

Amorphous CaF_2 systems were generated using the liquid quench technique (LQT), as described by Jung et al., which was implemented using AIMD.[23] These calculations were performed using a 400 eV plane-wave cutoff and a 1-fs time-step. The Brillouin zone was sampled with a $1 \times 1 \times 1$ *k*-point mesh. The atomic structures of amorphous CaF_2 are generated by the LQT, without any Ca metal present in this process. The (100) face of Ca is then joined with amorphous CaF_2 to generate the two-probe structure, which is then allowed to relax to its minimal energy state. This process is further described as follows: a cell of crystalline CaF_2 containing 96 atoms was heated to 2700 K, a value roughly 1000 K above the melting point of CaF_2, at a rate of 1 K/fs.[24] Then, the cell was allowed to equilibrate at that temperature for 10 ps, cooled to 300 K at a rate of 1 K/fs, and allowed to equilibrate at 300 K for 10 ps. Finally, a variable-cell relaxation of the system was performed. This process was done with cells consisting of 48 and 144 atoms in the stoichiometric arrangement of CaF_2 as well, in order to obtain amorphous CaF_2 cells of different thicknesses. The resulting amorphous CaF_2 cell was placed between Ca electrodes, and the same process of electrode straining and cell optimization was performed on the amorphous systems as was done for crystalline CaF_2. As well, the effects of randomization were considered: CaF_2 was allowed to equilibrate at the heated temperature for different amounts of time before cooling, resulting in different atomic structures of amorphous CaF_2. These structures are shown in Fig. S2 of the ESI.†

Polycrystalline structures were obtained using the aimsGB code developed by Cheng et al.[25] Two distinct CaF_2 polycrystalline cells were generated using the code: "mirror," and "twist," shown in Fig. 2(a) and Fig. 2(b), respectively. These systems were then joined with Ca electrodes and optimized as two-probe structures, as shown in Fig. 2(c-e).

Electron transport calculations were performed using the NanoDCAL code, which employs the non-equilibrium Green's function formalism in conjunction with density functional theory (NEGF-DFT) in order to calculate the transmission spectra across

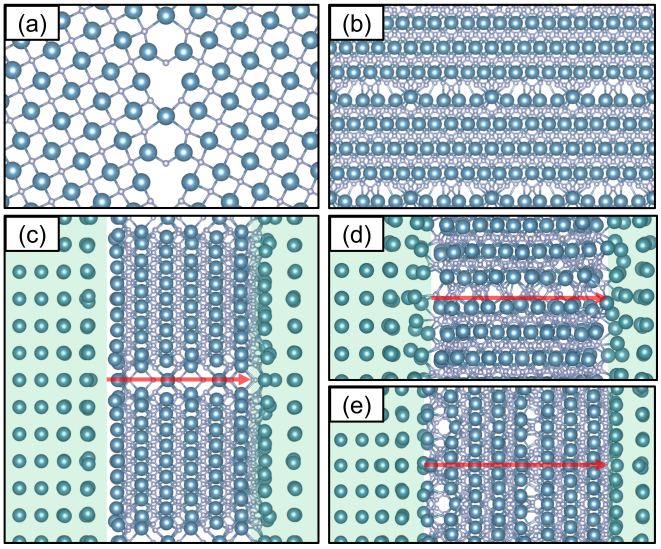

Fig. 2 Grain boundary systems studied in this work. (a) End view of mirror CaF_2, and (b) side view of twist CaF_2. (c) An example mirror parallel CaF_2 system sandwiched between Ca metal electrodes, (d) twist parallel CaF_2, (e) twist perpendicular CaF_2. The electrodes in (c)-(e) lie in the green shaded regions, and electron flow is directed along the red arrows with "parallel" and "perpendicular" referring to the grain boundary orientation relative to the direction of electron flow.

the simulation cell.[26,27] A key construct of NEGF-DFT formalism is the retarded Green's function,

$$G(E) = [(E + i\eta)S - H - \Sigma_1 - \Sigma_2]^{-1}, \quad (1)$$

where H and S are the Hamiltonian and overlap matrices for the scattering region, respectively, η is a positive infinitesimal, and $\Sigma_{1,2}$ are the self-energies that account for the broadening and energy shift effects of the left and right electrodes on the scattering region.[26]

The self-energies consist of both real and imaginary components. The real component represents a shift of the energy levels in the scattering region due to the electrodes, and the imaginary component represents the broadening of these levels due to the electrodes. The level broadening corresponds to the broadening matrix,

$$\Gamma_{1,2} = i(\Sigma_{1,2} - \Sigma_{1,2}^{\dagger}). \quad (2)$$

The self-energy is calculated by an iterative technique.[28] From these quantities, the electronic density matrix can be obtained as,

$$\rho = \frac{1}{2\pi}\int_{-\infty}^{\infty}[f(E,\mu_1)G\Gamma_1 G^{\dagger} + f(E,\mu_2)G\Gamma_2 G^{\dagger}]\,dE, \quad (3)$$

where $\mu_{1,2}$ are the electrochemical potentials of the left and right electrodes, and $f(E,\mu)$ is the Fermi-Dirac function, which describes the population of an energy level given the energy and electrochemical potential, μ. The bias voltage between the two electrodes is given by $eV_b = \mu_L - \mu_R$. The density obtained from Eq. 3 is used in a subsequent NEGF-DFT iteration step and the cycle is repeated until self-consistency is achieved in terms of the Hamiltonian and electron density. With the Green's function, the transmission function $T(E)$ can now be obtained as,

$$T(E) = (\Gamma_1 G \Gamma_2 G^{\dagger}), \quad (4)$$

which represents the probability that an electron with a given energy E will transmit from one electrode, through the scattering region, and into the other electrode.[29]

3 Results and Discussion

The partial density of states (PDOS) plots of all amorphous, polycrystalline, and crystalline systems without electrodes were calculated, as shown in Fig. 3, in order to make initial predictions about electron conductance. All systems show a band gap larger than 6 eV, implying that these CaF_2 systems are insulating in nature. The reported experimental band gap of bulk CaF_2 is 12 eV, quite different from the values presented here.[30,31] However, our result of 7.20 eV for bulk CaF_2 is in good agreement with previous DFT studies.[32,33] DFT is known to underestimate band gaps, and special functionals must be used to obtain band gaps consistent with experiment.[34] Unfortunately, these functionals are not available for NEGF-DFT calculations.[26] These results are expected and common in computational studies. The calculated band gaps differ between crystalline, amorphous, and polycrystalline systems, suggesting that the systems under investigation have different electron transport properties. This will be investigated further via the transmission spectra of each system. A summary of each system and its associated band gap can be found in Table S1 in the ESI.† Amorphous systems possess band gaps that are 0.3-0.5 eV smaller than the crystalline systems. As well, the mirror parallel and twist grain boundaries have band gaps that are 1.0-1.2 eV smaller than crystalline CaF_2. States existing within the grain boundary of the mirror parallel system are responsible for the narrowing of the band gap, causing the peak at 6-7 eV in the PDOS of this system. A description of this phenomena can be found in Section S4 of the ESI.† Through these data, we could assume that amorphous and polycrystalline systems have a higher probability of electron tunneling than crystalline CaF_2. However, the band gaps alone will not adequately describe electron transport through these systems. To further investigate this, the transmission spectra of each system was calculated using the non-equilibrium Green's Function technique.

The transmission spectra for varying thicknesses of crystalline CaF_2 are plotted in Fig. 4. Bulk Ca is shown on this graph as a reference, and shows relatively high transmission across the entire energy range. The transmission functions of all crystalline systems near the Fermi energy (E_F) of the Ca metal electrodes are orders of magnitude lower than that of pure Ca. However, the transmission function of CaF_2 (8.8 Å) is noticeably higher than other CaF_2 systems. This is particularly prominant at E_F, where the gap between the transmission function of CaF_2 (8.8 Å) and CaF_2 (14.3 Å) is greater than between any other pair of crystalline CaF_2 systems. This is due to the fact that the electrodes are close enough to each other that some of the insulating nature of the CaF_2 can be overcome by the metallic nature of the electrodes. Scattering state plots help illustrate this and were calculated for each system at E_F; these data are shown Fig. S4.†

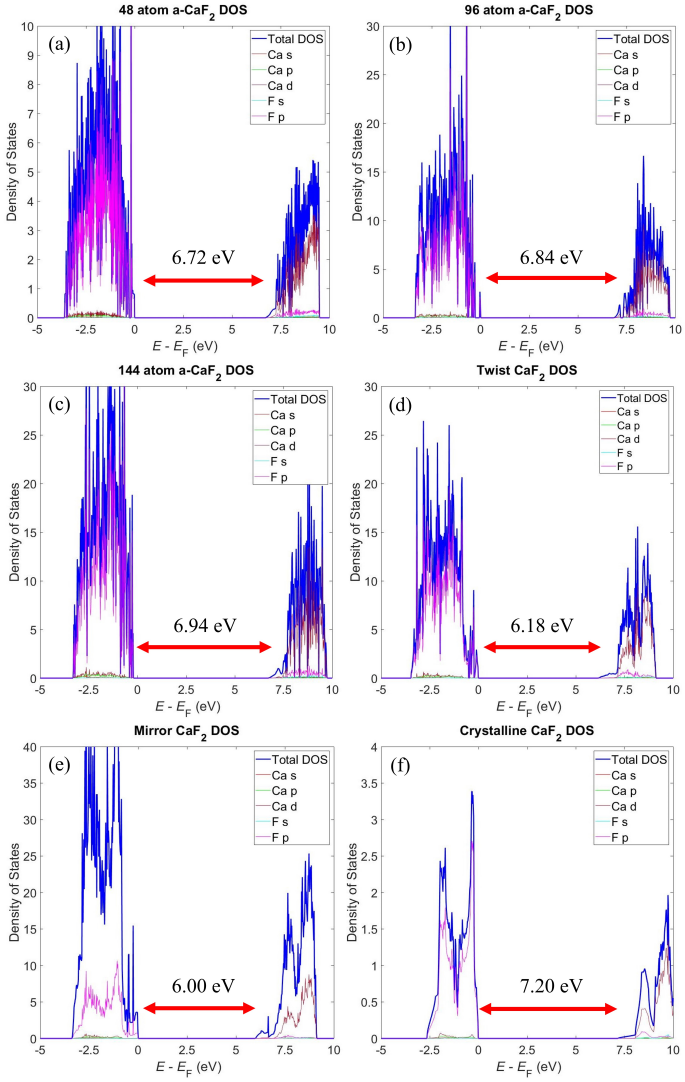

Fig. 3 Partial density of states for various CaF_2 systems: amorphous CaF_2 with (a) 48, (b) 96, and (c) 144 atoms, polycrystalline CaF_2 in (d) twist and (e) mirror parallel arrangements and (f) crystalline CaF_2. The red arrows show the band gap.

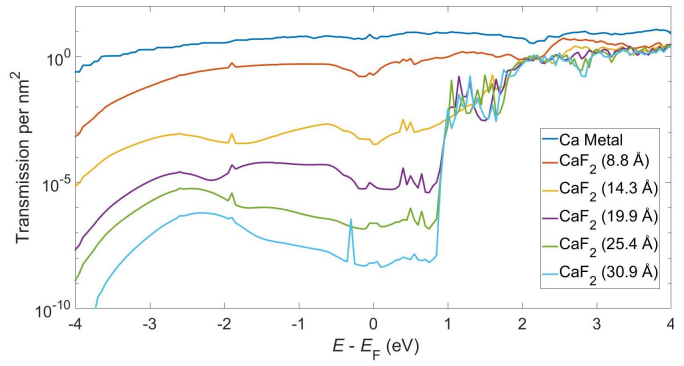

Fig. 4 Transmission spectra of increasing thicknesses of crystalline CaF_2 plotted on a logarithmic scale.

The transmission function of crystalline CaF_2 decreases by several orders of magnitude as thickness increases, most noticeably at the Fermi energy of the electrodes. The value of the transmission function at E_F is known as the low-bias conductance, and the rate at which the low-bias conductance decays as thickness increases is key for extrapolating our computed values to SEI layer thicknesses seen in experiment. This rate of decay also allows for the direct comparison of the insulating properties of crystalline CaF_2 to those of amorphous and polycrystalline CaF_2. Systems with a larger rate of low-bias conductance decay will protect the electrolyte from decomposition more effectively than will systems with a smaller rate of low-bias conductance decay as the SEI layer thickness grows during battery operation.

The transmission spectra for varying thicknesses of amorphous CaF_2, as well as bulk Ca as a reference, are plotted in Fig. 5. Order-of-magnitude decreases in the transmission spectra at the Fermi energy of the electrodes are observed as the thickness of the amorphous CaF_2 layer increases. However, amorphous materials of the same thickness may have differing atomic structures that could have an effect on electron transport across the system. Therefore, the effects that differing atomic structures have on electron transmission must also be investigated.

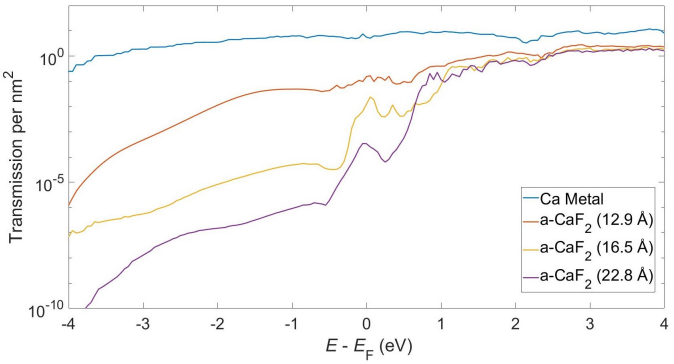

Fig. 5 Transmission spectra of amorphous CaF_2 of increasing thickness on a logarithmic scale.

A comparison of the transmission spectra of different amorphous atomic structures consisting of 96 atoms in the stoichiometric formula of CaF_2 was conducted. The process is described in Section S2 of the ESI.† The transmission spectra of these systems were then calculated, as shown in Fig 6, and compared to the original amorphous CaF_2 structure. The average transmission spectra of all different structures was calculated from these data. AS-1, AS-3, AS-4, AS-5, AS-6, and the original a-CaF_2 systems show very similar behaviors at E_F and above, while AS-2 differs in these regions. The original a-CaF_2 system slightly differs from all other structures at energies below E_F.

AS-2 displays the most marked difference out of all atomic structures. After the process of electrode-system structural optimization, we noticed that the electrode-CaF_2 separation distance in AS-2 is greater than in other atomic structures. The optimized *c* vector of AS-2 was 30.7 Å , while the optimized *c* vectors of AS-1,3,5, and 6 were all 30.4 Å. AS-4 had an optimized *c* vector of 30.3 Å, and the original system had an optimized *c*-vector of 31.1 Å. The elongated AS-2 *c*-vector partially explains the behavior of the transmission function of AS-2 in Fig. 6. However, the original structure also has a longer *c*-vector than most other

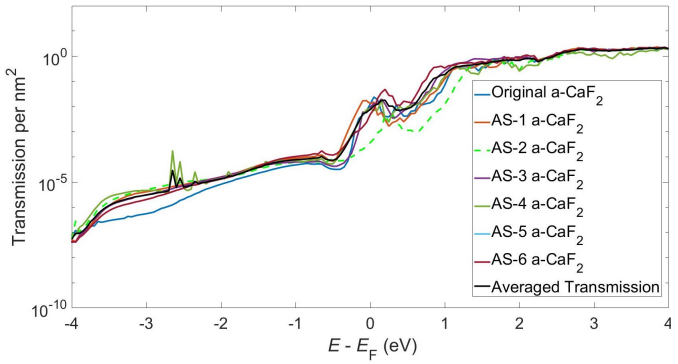

Fig. 6 The transmission spectra of different atomic structures of amorphous CaF_2 on a logarithmic scale.

atomic structures, yet does not exhibit the same decreased transmission function as AS-2. This can be explained by investigating the structures, as shown in Figs. S2 and S5.† AS-2 has a significant void between the left electrode and CaF_2, while all other amorphous systems do not exhibit the same gap between the electrodes and CaF_2. The combined affects of increased c-vector length and the void between the left electrode and CaF_2 are responsible for the marked difference in the transmission spectra of AS-2, while the increased c-vector length of the original system is responsible for the difference in the transmission function of the original system at energies below -1 eV. The averaged zero-bias conductance of all amorphous structures was calculated to be 9.7×10^{-3} G_0, and the standard deviation was calculated to be 5.2×10^{-3} G_0. These results indicate that the original low-bias conductance obtained from the transmission data in Fig. 5 can be used to compare the insulating properties of amorphous CaF_2 to crystalline and polycrystalline phase CaF_2.

Fig. 7(a) shows the transmission of bulk Ca as well as 3 thicknesses of mirror parallel CaF_2. Fig. 7(b) shows the transmission of bulk Ca, two different thicknesses of twist parallel CaF_2, and one thickness of twist perpendicular CaF_2. Electron transmission decreases exponentially at energies near E_F as the thickness of the mirror parallel systems increases. The calculated transmission spectra of twist parallel CaF_2 also decreases exponentially with increasing thickness, and the 28-Å thick twist perpendicular system shows a transmission spectrum about an order of magnitude lower than the 20-Å thick twist parallel system.

The crux of our results, the low-bias conductance, best describes the ability of a system to conduct electrons in the limit of zero bias voltage, and is important for determining which systems best protect against electron leakage from the anode. Conductance is known to scale as $G \propto e^{-\beta n}$, where n is the CaF_2 layer thickness and β is the decay constant.[35,36] Obtaining the value of the decay constant β allows for the prediction of low-bias conductance in thicker films. The low-bias conductance was calculated for each thickness of each system (crystalline, amorphous, and polycrystalline), as well as for metallic calcium. These data are shown in Fig. 8, and numerical values of the low-bias conductance of each system can be found in Table S2.† From Fig. 8, it is evident that amorphous CaF_2 has far higher conductance than crystalline CaF_2 at similar thicknesses. As well,

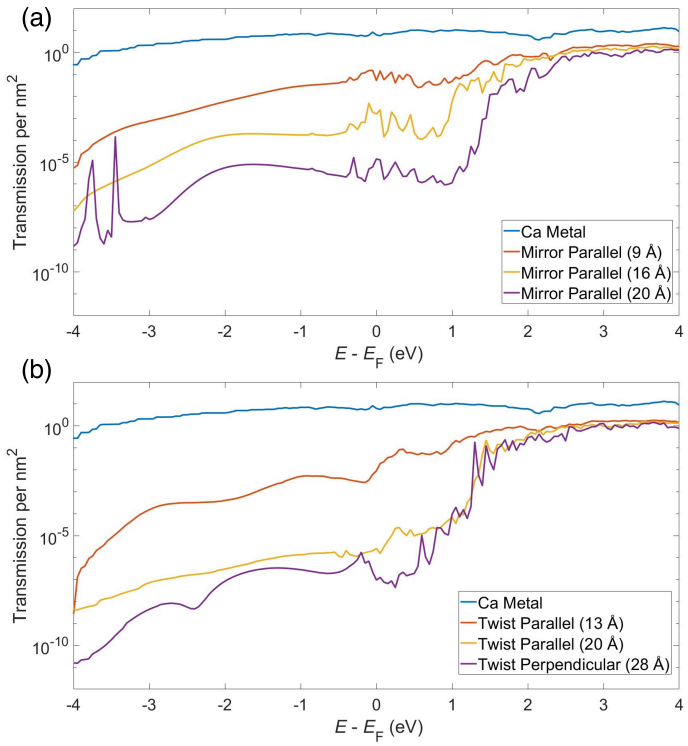

Fig. 7 (a) Transmission spectra of pure calcium, 9-Å thick, 16-Å thick, and 20-Å thick mirror parallel CaF_2 systems. (b) Transmission spectra of pure calcium, 13-Å thick and 20-Å thick twist parallel CaF_2, and 28-Å thick twist perpendicular CaF_2.

the low-bias conductance of crystalline CaF_2 has a sharper decay than amorphous CaF_2 as layer thickness increases. The mirror parallel system shows a conductance trend similar to crystalline CaF_2 with a slight variation between the systems around 15-Å of CaF_2 layer thickness. The parallel twist system also shows a similar conductance trend to crystalline CaF_2, and the perpendicular twist system has a calculated conductance similar to crystalline CaF_2 as well. While the polycrystalline systems exhibit slightly higher conductance values than crystalline systems at certain thicknesses, the conductance values of these systems are still orders of magnitude lower than amorphous systems of similar thicknesses.

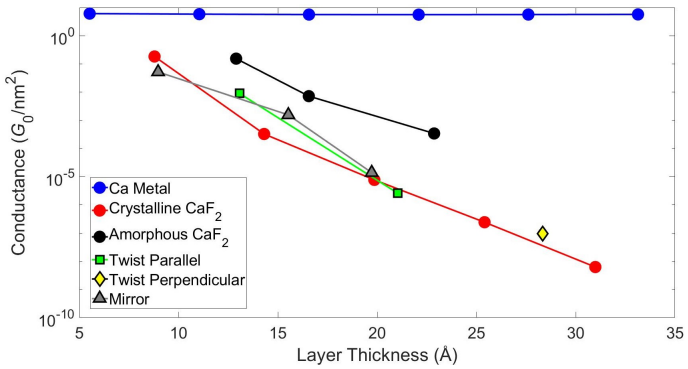

Fig. 8 Low-bias conductance of amorphous, crystalline, and polycrystalline systems of different thicknesses.

From these data the decay constant, β, was determined for the crystalline, amorphous, and polycrystalline phases of CaF_2 via an exponential fit. The decay constant of crystalline CaF_2 was determined to be 0.649 $Å^{-1}$, excluding the first datum from CaF_2 (8.8 Å). Using all data points, the β value of amorphous CaF_2 was calculated to be 0.599 $Å^{-1}$, and the β calculated for mirror parallel and twist parallel CaF_2 were obtained as 0.744 $Å^{-1}$ and 1.022 $Å^{-1}$, respectively. Given the greater β values of crystalline and polycrystalline CaF_2, it can be predicted that these systems will prevent electron leakage from the anode more effectively than amorphous CaF_2.

In order to adequately block electrons, inorganic, crystalline SEI films need to be >4 nm thick.[37] By extending the exponential fit function to 4 nm using the β values obtained from our calculations, order-of-magnitude predictions can be made about the conductance of 4-nm thick films of amorphous, crystalline, and polycrystalline CaF_2. At a thickness of 4 nm, the conductance values of amorphous, crystalline, twist parallel, and mirror parallel CaF_2 are expected to be 10^{-9} G_0/nm^2, 10^{-11} G_0/nm^2, 10^{-14} G_0/nm^2, and 10^{-12} G_0/nm^2, respectively. From these data, we are able to quantitatively compare the performance of crystalline, amorphous, and polycrystalline phases of CaF_2. Twist parallel is predicted to possess the lowest electronic conductance, whereas amorphous CaF_2 is predicted to possess the highest electronic conductance. From the comparison seen in Fig. 8, we conclude that crystalline and polycrystalline phase CaF_2 block electron transport more thoroughly than amorphous phase CaF_2. It should be emphasized that this work considers charge transport in the ballistic regime, modeling the tunneling of electrons through the CaF_2 region. Although this description provides great insight into charge transport through the system, other mechanisms are likely to occur, such as charge hopping. These other processes must be treated with other computational approaches and will provide fascinating follow-up studies. Future investigations will analyze electron transport through other grain boundary structures, although these data give early indications that polycrystalline systems possess electron blocking properties comparable to crystalline systems, and that these systems are better at stemming electron flow from the anode than amorphous CaF_2.

Conclusions

In conclusion, we performed NEGF-DFT electron transport calculations on crystalline, amorphous, and polycrystalline CaF_2, modelling a broad spectrum of different phases of the prototypical SEI component CaF_2. While all systems were insulating, the amorphous CaF_2 systems exhibited conductance values one to two orders of magnitude higher than the crystalline systems at comparable thicknesses. Surprisingly, our NEGF-DFT calculations predict that polycrystalline systems have comparable electron blocking properties to crystalline systems. These results highlight the important role that different phases of the same material have on the performance of the SEI, and provide insights as to how to best stem electron flow from the anode. However, these results also promote questions that can be investigated in future studies, such as evaluating how the conductance of CaF_2 evolves with time, or how the inclusion of electric fields and electron-phonon scattering affect the transport properties of CaF_2. The information presented here lays the groundwork for future investigations into this material and provides the potential to help the realization of a calcium-ion battery.

Conflicts of interest

There are no conflicts to declare.

Acknowledgements

K.B. and M.S. were supported by funds from Binghamton University. DFT calculations were performed using the CARBON cluster at the Center for Nanoscale Materials (Argonne National Laboratory, supported by the U.S. DOE, Office of Basic Energy Sciences (BES), DE-AC02-06CH11357) under allocation CNM72207, and the Spiedie cluster at Binghamton University.

Notes and references

1 A. Y. Tsivadze, T. Kulova and A. Skundin, *Prot. Met. Phys. Chem. Surf.*, 2013, **49**, 145–150.
2 B. Scrosati and J. Garche, *J. Power Sources*, 2010, **195**, 2419–2430.
3 C. Xu, Y. Chen, S. Shi, J. Li, F. Kang and D. Su, *Sci. Rep*, 2015, **5**, 14120.
4 A. Ponrouch and M. Palacin, *Current Opinion in Electrochemistry*, 2018, **9**, 1–7.
5 R. Guduru and J. Icaza, *Nanomat.*, 2016, **6**, 41.
6 A. Yarosheysky, *Geochem. Intern.*, 2006, **44**, 48–55.
7 M. Yoshio, R. Brodd and A. Kozawa, *Lithium-Ion Batteries*, Springer-Verlag, New York City, 1st edn, 2009.
8 R. J. Gummow, G. Vamvounis, M. B. Kannan and Y. He, *Advanced Mat.*, 2018, **30**, 1–14.
9 E. Peled and S. Menkin, *J. Electrochem. Soc.*, 2017, **164**, A1703–A1719.
10 J. Young and M. Smeu, *J. Phys. Chem. Lett.*, 2018, **9**, 3295–3300.
11 J. Young, P. Kulick, T. Juran and M. Smeu, *ACS Appl. Energy. Mater.*, 2019, **2**, 1676–1684.
12 M. Elena Arroyo-de Dompablo, A. Ponrouch, P. Johansson and M. Rosa Palacín, *Chem. Rev.*, 2020, **120**, 6331–6357.
13 M. Smeu and K. Leung, *Phys. Chem. Chem. Phys.*, 2021, **23**, 3214–3218.
14 R. Car and M. Parrinello, *Phys. Rev. Lett.*, 1985, **55**, 2471–2474.
15 G. Kresse and J. Furthmüller, *Comput. Mater. Sci.*, 1996, **6**, 15–50.
16 G. Kresse and J. Furthmüller, *Phys. Rev. B*, 1996, **54**, 11169.
17 G. Kresse and J. Hafner, *Phys. Rev. B*, 1993, **47**, 558–561.
18 P. Blöchl, *Phys. Rev. B*, 1994, **50**, 17953.
19 J. Perdew, A. Ruzsinszky, O. Csonka, G.I. Vydrov, L. Scuseria, G.E. Constantin, X. Zhou and K. Burke, *Phys. Rev. Lett.*, 2008, **100**, 1–4.
20 A. Jain, S. P. Ong, G. Hautier, W. Chen, W. D. Richards, S. Dacek, S. Cholia, D. Gunter, D. Skinner, G. Ceder and K. a. Persson, *APL Mater.*, 2013, **1**, 011002.

21 K. Leung and A. Leenheer, *J. Phys. Chem. C*, 2015, **119**, 10234–10246.

22 K. Leung, *Phys. Chem. Chem. Phys.*, 2020, **22**, 10412.

23 S. Jung, H. Kim, J. Choi and Y. Han, *Nano. Lett.*, 2014, **14**, 6559–6563.

24 S. Budavari, *The Merck Index - An Encyclopedia of Chemicals, Drugs, and Biologicals*, Merck and Co., Inc., Whitehouse Station, NJ, 1996.

25 J. Cheng, J. Luo and K. Yang, *Comp. Mat. Sci.*, 2018, **155**, 92–103.

26 J. Taylor, H. Guo and J. Wang, *Phys. Rev. B*, 2001, **63**, 245407.

27 D. Waldron, P. Haney, B. Larade, A. MacDonald and H. Guo, *Phys. Rev. Lett.*, 2006, **96**, 166804.

28 M. Sancho, J. Sancho and J. Rubio, *J. Phys. F: Met. Phys*, 1984, **14**, 1205–1215.

29 M. Smeu and G. DiLabio, *J. Phys. Chem. C*, 2010, **115**, 17874–17879.

30 C. Görling, U. Leinhos and K. Mann, *Opt. Commun.*, 2005, **249**, 319–328.

31 G. W. Rubloff, *Phys. Rev. B*, 1972, **5**, 662.

32 H. Shi, R. Eglitis and G. Borstel, *Phys. Stat. Sol.*, 2005, **242**, 2041–2050.

33 H. Shi, W. Luo, B. Johansson and R. Ahujia, *J. Phys.: Condens. Matter*, 2009, **21**, 415501.

34 U. Salzner, P. Pickup, R. Poirier and J. Lagowski, *J. Phys. Chem. A*, 1998, **102**, 2572–2578.

35 C. Joachim, J. Gimzewski and A. Aviram, *Nature*, 2000, **408**, 541–548.

36 T. Tada and K. Yoshizawa, *Phys. Chem. Chem. Phys.*, 2015, **17**, 32099.

37 K. Leung, Y. Qi, K. Zavadil, Y. Jung, A. Dillon, A. Cavanagh, S. Lee and S. George, *J. Am. Chem. Soc.*, 2011, **133**, 14741–14754.